Available online at www.sciencedirect.com

SCIENCE DIRECT®

International Journal of Heat and Fluid Flow 26 (2005) 244–255

International Journal of HEAT AND FLUID FLOW

www.elsevier.com/locate/ijhff

Simulation and measurement of flow and heat transfer in two planar impinging jets

T. Akiyama [a], K. Yamamoto [a], K.D. Squires [b], K. Hishida [a,*]

[a] *Department of System Design Engineering, Faculty of Science and Technology, Keio University, 3-14-1 Hiyoshi, Kouhoku-ku, Yokohama 223-8522, Japan*

[b] *Department of Mechanical and Aerospace Engineering, Arizona State University, Tempe, AZ 85287-6106, USA*

Received 11 March 2004; accepted 2 August 2004
Available online 8 October 2004

Abstract

The flow and heat transfer in two planar impinging jets are investigated using Large-Eddy simulation and experiments. The jet Reynolds number based on nozzle width and centerline velocity is 500. Predictions are obtained of unforced jets in addition to forced cases in which periodic injection and suction is applied at the nozzle exit of each jet. The goal of the current effort is to characterize the predictions of the flow from the numerical simulations prior to future efforts aimed at applying techniques to control the heat transfer on the impinging wall. Forcing results in significant changes to the flow structure with a rapid development of large-scale vortices in the shear layers emerging from the nozzle, which does not occur in the unforced jets. For both the forced and unforced flows, spanwise vorticity is apparent in the structure of the wall jet that forms as the flow develops near and along the impingement surface. The influence of the forcing raises the local Nusselt number in the vicinity of the stagnation line by about 10% compared to the unforced case.

Keywords: Impinging jet; Heat transfer; PIV Measurement; Large-Eddy simulation

1. Introduction

Heat transfer in impinging jets is superior to that achieved by typical convective approaches because high heat transfer rates are possible in the stagnation region beneath the jets. Use of impinging jets in applications is straightforward, e.g., the relative ease in focusing jets onto a particular region of interest. For these and other reasons, impinging jet cooling/heating techniques are widely used in many industrial systems such as cooling of high temperature gas turbines, drying of paper or textiles, processing of steel or glass, and increasingly as a means to cool electrical equipment. Consequently, heat transfer and fluid flow characteristics in such flows are an important topic of scientific and engineering interest.

The work reported below is the first step in a larger program aimed at development of techniques to control surface heat transfer characteristics using planar, impinging jets. Increasingly, many applications, e.g., in materials processing, require high-precision approaches capable of local control of system response. The longer-term interest of the present research includes passive application of static disturbances (e.g., alteration of the nozzle configuration) as well as active techniques such as the use of actuators.

For heat transfer applications using impinging jets, an important consideration is the ability to achieve and control a relatively wide range in heat transfer rates and distributions. For a single impinging jet, the flexibility in the spatial distribution possible in heat transfer is limited—changes in the relative spatial distribution

---

[*] Corresponding author. Tel.: +81 45 563 1141; fax: +81 45 566 1739.
E-mail address: hishida@sd.keio.ac.jp (K. Hishida).

0142-727X/$ - see front matter © 2004 Elsevier Inc. All rights reserved.
doi:10.1016/j.ijheatfluidflow.2004.08.005

Nomenclature

B	nozzle width
C	square of the Smagorinsky constant
c_p	specific heat at constant pressure
H	the distance between the nozzle and impinging wall
h_j	SGS heat flux
Nu	Nusselt number
Pr	Prandtl number
Pr_{sgs}	SGS Prandtl number
q_{wall}	heat flux through impinging wall
Re	Reynolds number
s	nozzle spacing
$\overline{S}_{ij}$	strain rate tensor on the grid level
$\widetilde{\overline{S}}_{ij}$	strain rate tensor on the test level
St	Strouhal number based on nozzle width
St_ζ	Strouhal number based on momentum thickness

T	temperature
t	time
U_0	mean inlet velocity
U_c	convective velocity on outlet
u_i	velocity
Greeks	
α	filter ratio
$\overline{\Delta}$	a grid filter width
$\widetilde{\overline{\Delta}}$	test filter width
θ	non-dimensional temperature
ζ	momentum thickness
κ	wave number
κ_0	peak wave number
ρ	density
ω_x, ω_y, ω_z	vorticity components

along the surface beneath a single impinging jet are not easily achieved. The use of multiple jets is attractive as a means to add degrees of freedom to a control input and in turn enable greater variation in the spatial distribution of the heat transfer along the impinging surface. Dual jet configurations are a logical step towards multiple-jet configurations. Characterization of the flow and heat transfer of two planar impinging jets are the focus of this study.

The approach adopted in this work is a combination of experimental measurements and Large-Eddy simulation (LES). A simulation tool such as LES is motivated as a means to describe in detail the underlying features of the flow and for eventually testing flow-control approaches. Design of control laws requires knowledge of the time-dependent variation of heat transfer rates and flow properties since control inputs change in time in response to the current output, i.e., state of the flow. In LES the time-dependent and three-dimensional evolution of the large scales are explicitly computed and it is of interest to use the LES predictions to provide descriptions that might eventually be useful for controller design.

Most previous work on fluid flow and/or heat transfer characteristics has focused on single jet impingement (e.g., see Baughn and Shimizu, 1989; Lytle and Webb, 1994; Sakakibara et al., 1997; Sakakibara et al., 2001). These and related studies show that flows are complex, e.g., characterized by entrainment, stagnation, streamline curvature, and that measurements can be sensitive to the details of the configuration and turbulence conditions. These factors includes effects such as H/B, the ratio of the distance from the jet exit to the impinging surface to the nozzle width, and the jet Reynolds number, for example. Sakakibara et al. (1997) and Sakakibara et al. (2001) have shown that the vortical structure that develops in the vicinity of the stagnation line (symmetry line for a single jet) influences the heat transfer on the impinging surface. These investigators identified the development and role of both spanwise structures and streamwise vortices that developed in the jet and over the impinging wall. In this study, the ratio H/B is relatively small, consistent with the long-term aims in control for which small H/B is advantageous in that surface distributions should be more directly influenced by actuation at the nozzle. The spacing between the nozzles of dual jets is an additional parameter compared to single-jet configurations and is comparable to H/B in the present study.

Jet impingement is a challenging test case for Reynolds-averaged Navier–Stokes (RANS) turbulence models with complications arising from the development of Reynolds stress anisotropy and response of the models in the stagnation region. Some of the most widely applied closures such as k–ε, for example, substantially over-predict heat transfer rates on the impinging surface. While there is notable progress in RANS modeling in impinging jets reported by Behnia et al. (1999), the general shortcomings of RANS models in heat transfer applications and given the interest in flow-control strategies, techniques that directly compute all, or most, of the time-dependent turbulent motions are motivated.

Reported below are the investigations of the flow and heat transfer characteristics beneath dual, planar impinging jets. The system is characterized using LES predictions and LDV and PIV measurements in both a natural flow and in a second case with forcing introduced via periodic injection and suction at both sides of the exit of each nozzle. It is well known that the natural instabilities of jets can be amplified by forcing techniques applied near or at the jet/nozzle exit, in turn altering overall flow characteristics (e.g., see Crow and Champagne, 1971; Zaman and Hussain, 1981; Liu and Sullivan, 1996; Hwang and Cho, 2003). Thus, one of the aims of the study is to investigate the contrast between the two flow types.

2. Configuration and approach

The configuration considered is that of two planar impinging jets with a nozzle spacing of $s/B = 3.6$, where s is the spacing between the nozzle centers and B is the width of the nozzle exit. The Reynolds number, Re, of each of the two jets based on the jet centerline velocity U_0 and B are 500 and the distance from the jet exit to the impinging wall is $H/B = 4$. The working fluid is water in the experiments, a molecular Prandtl number of 7.0 is employed in the simulations. The coordinate system is illustrated in Fig. 1(a) and nozzle configuration in Fig. 1(b). Note that the primary flow is initially along the x-axis (towards the impinging wall) with the flow turned outwards and developing as a wall jet with the main flow direction along the y-axis. The geometry and flow parameters for the present study are the same as in the experiments reported by Yamamoto et al. (2002). Following Sakakibara et al. (2001), a co-flow is imposed in order to eliminate recirculation and ensure a supply of fluid for jet entrainment. The co-flow is directed along the x-axis, is uniform over the y–z plane, and has a magnitude of $0.05U_0$ (c.f., Fig. 1(b)). Forcing of the jets is accomplished using injection and suction, introduced at an angle of 45° to the nozzle exit plane as shown in the figure. The computational domain measures $4B \times 52B \times 3B$ (in x, y, z). The impinging wall is heated and a spatially-uniform and constant heat flux is prescribed.

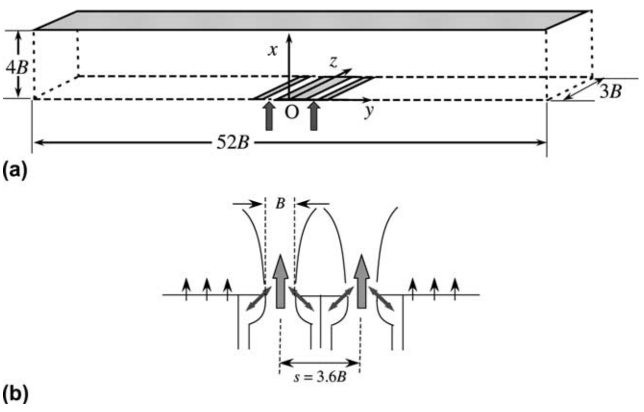

Fig. 1. Flow schematic in two planar impinging jets: (a) computational domain and coordinate system and (b) nozzle configuration.

2.1. Governing equations and turbulence models

The flow is governed by the filtered incompressible mass conservation equation,

$$\frac{\partial \overline{u}_i}{\partial x_i} = 0 \tag{1}$$

the filtered incompressible Navier–Stokes equations

$$\frac{\partial \overline{u}_i}{\partial t} + \frac{\partial \overline{u}_i \overline{u}_j}{\partial x_j} = -\frac{\partial \overline{P}}{\partial x_i} + \frac{1}{Re}\frac{\partial^2 \overline{u}_i}{\partial x_j \partial x_j} - \frac{\partial \tau_{ij}}{\partial x_j}, \tag{2}$$

where $\tau_{ij} = \overline{u_i u_j} - \overline{u}_i \overline{u}_j$ is the sub-grid scale stress, and the filtered energy equation

$$\frac{\partial \overline{\theta}}{\partial t} + \frac{\partial \overline{\theta}\overline{u}_j}{\partial x_j} = \frac{1}{RePr}\frac{\partial^2 \overline{\theta}}{\partial x_j \partial x_j} - \frac{\partial h_j}{\partial x_j}, \tag{3}$$

where $h_j = \overline{\theta u_j} - \overline{\theta}\overline{u}_j$ is the sub-grid scale heat flux. The governing equations as written have been made dimensionless using length and velocity scales corresponding to the nozzle width B and jet centerline velocity U_0, respectively. The dimensionless temperature θ in (3) is defined as

$$\theta = \frac{\Delta T \rho c_p U_0}{q_{\text{wall}}}, \quad \Delta T = T(x_k, t) - T_{\text{bulk}} \tag{4}$$

where $T(x_k,t)$ is the temperature of the fluid and T_{bulk} is the bulk temperature in the jets entering the domain. The prescribed wall heat flux is q_{wall}. The specific heat at constant pressure is denoted c_p above and ρ is the fluid density.

The sub-grid scale stress is closed using the dynamic Smagorinsky model proposed by Germano et al. (1991). The square of the Smagorinsky constant $C(= C_s^2)$ and sub-grid scale Prandtl number Pr_{sgs} are computed during the course of the simulation. The eddy-viscosity assumptions leads to the expressions

$$\tau_{ij} - \tfrac{1}{3}\tau_{kk}\delta_{ij} = -2C\overline{\Delta}^2 \mid \overline{S} \mid \overline{S}_{ij}, \tag{5}$$

$$h_j = -CPr_{\text{sgs}}^{-1}\overline{\Delta}^2 \mid \overline{S} \mid \frac{\partial \overline{\theta}}{\partial x_j}. \tag{6}$$

In the dynamic procedure, a second filtering is introduced with the filter-width ratio $\alpha = \widetilde{\overline{\Delta}}/\overline{\Delta} = 2$ utilized for the present simulations, with $\widetilde{\overline{\Delta}}$ representing the test filter width. The model coefficient is calculated using the least squares approach proposed by Lilly (1992),

$$C = \frac{\langle L_{ij} M_{ij}\rangle}{\langle M_{kl} M_{kl}\rangle}. \tag{7}$$

In this work L_{ij} and M_{ij} are approximated using Taylor series expansions following Chester et al. (2001):

$$L_{ij} = \frac{(\alpha\overline{\Delta})^2}{12}\frac{\partial \overline{u}_i}{\partial x_k}\frac{\partial \overline{u}_j}{\partial x_k} + \mathrm{O}(\overline{\Delta}^4), \tag{8}$$

$$M_{ij} = 2\overline{\Delta}^2 \left\{ \left(| \overline{S} | \overline{S}_{ij} - \alpha^2 | \widetilde{\overline{S}} | \overline{S}_{ij} \right) + \frac{(\alpha \overline{\Delta}^2)}{24} \left[\nabla^2 (| \overline{S} | \overline{S}_{ij}) - \alpha^2 | \widetilde{\overline{S}} | \nabla^2 \overline{S}_{ij} \right] + \mathrm{O}(\overline{\Delta}^4) \right\}, \tag{9}$$

where $| \widetilde{\overline{S}} |$ is the derivative-based approximation

$$| \widetilde{\overline{S}} | = \sqrt{2 \left(\overline{S}_{ij} + \frac{(\alpha \overline{\Delta})^2}{24} \nabla^2 \overline{S}_{ij} \right)^2} \tag{10}$$

using the second-order expansions. The sub-grid Prandtl number, Pr_{sgs}, is obtained from analogous relations

$$Pr_{\mathrm{sgs}}^{-1} = C^{-1} \frac{\langle P_j R_j \rangle}{\langle R_k^2 \rangle}, \tag{11}$$

$$P_j = \frac{(\alpha \overline{\Delta})^2}{12} \frac{\partial \overline{\theta}}{\partial x_k} \frac{\partial \bar{u}_j}{\partial x_k} + \mathrm{O}(\overline{\Delta}^4), \tag{12}$$

$$R_j = \overline{\Delta}^2 \left\{ \left(| \overline{S} | \frac{\partial \overline{\theta}}{\partial x_j} - \alpha^2 | \widetilde{\overline{S}} | \frac{\partial \overline{\theta}}{\partial x_j} \right) + \frac{(\alpha \overline{\Delta}^2)}{24} \times \left[\nabla^2 \left(| \overline{S} | \frac{\partial \overline{\theta}}{\partial x_j} \right) - \alpha^2 | \widetilde{\overline{S}} | \nabla^2 \left(\frac{\partial \overline{\theta}}{\partial x_j} \right) + \mathrm{O}(\overline{\Delta}^4) \right] \right\}. \tag{13}$$

The averages indicated in the above expressions for the sub-grid model co-efficients (7) and (11) are the statistically homogeneous spanwise direction, an undesirable though necessary procedure to prevent numerical instabilities which arise from a point-by-point application of the previous relations and caused by negative values of C and/or Pr_{sgs}. The negative values of the model coefficients are indicative of regions in which a reverse transfer of energy (backscatter) from the sub-grid to the resolved scales of motion is predicted. Thus, averaging the coefficients allows the effect of backscatter to be accounted for, albeit in an average sense, and probably somewhat roughly given the simple closures applied for the sub-grid stress and heat flux. Following the spanwise averaging, if the model coefficients remained negative the values were truncated to zero.

2.2. Numerical procedures

Solutions were obtained on a non-uniform staggered Cartesian grid using a fractional step method. Solution of the Poisson equation for pressure was accomplished using symmetric SOR. For most of the results reported below, the grid was comprised of 64 × 192 × 32 points in the x, y, z directions, respectively. As shown in Fig. 2, the grid spacings were non-uniform in the x and y directions in order to resolve the variations in the solution near solid surfaces and in the jet shear layers. In the statistically homogeneous spanwise z direction, a uniform grid was employed.

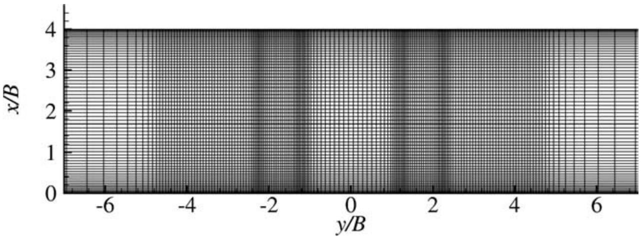

Fig. 2. Zoomed view of grid configuration in the vicinity of the nozzle exit.

Centered, second-order accurate differences were used to approximate the spatial derivatives in the momentum equations, the particular form employed conserving momentum and kinetic energy on non-uniform grids (Kajishima, 1999). The advection terms in the energy equation were approximated using a second-order accurate QUICK scheme (Leonard, 1979), with centered second-order differences applied to the remaining terms. Time integration is accomplished using the second-order Adams–Bashforth method. The maximum Courant number was less than 0.2 throughout any given run.

2.3. Boundary conditions

On the impinging wall, a no-slip condition was applied to the velocity components and a constant heat flux condition corresponding to a heated plate for the thermal energy equation. The time-dependent conditions of each velocity component and the temperature along the outlet boundary at $|y/B| = 26$ are obtained from the following convective conditions:

$$\frac{\partial \bar{u}_i}{\partial t} + U_{\mathrm{c}} \frac{\partial \bar{u}_i}{\partial y} = 0, \quad \frac{\partial \overline{\theta}}{\partial t} + U_{\mathrm{c}} \frac{\partial \overline{\theta}}{\partial y} = 0, \tag{14}$$

where U_{c} is the convection velocity that varies in time and is spatially-uniform along the outlet planes. Periodic boundary conditions are applied along the z-direction. Finally, along the inflow planes corresponding to the two jets ($x/B = 0$), the temperature is constant and velocity field is specified as outlined below.

2.4. Inflow condition

The mean velocity in the shear layers of the jet at the inflow plane is prescribed using a hyperbolic tangent profile

$$U(y) = \frac{U_0 - U_{\mathrm{e}}}{2} \left\{ 1 + \tanh \left(\frac{0.5B - | \xi |}{2\zeta} \right) \right\} + U_{\mathrm{e}}, \quad \xi = y - Y_{\mathrm{c}}, \tag{15}$$

where Y_c is the center position of the nozzle, ζ is the shear layer momentum thickness of $0.05B$, and U_e is the prescribed co-flow velocity of $0.05U_0$. Time-dependent velocity fluctuations $u_i'(y,z,t)$ are added to the mean profile (15). The fluctuations are generated from a prescribed radial energy spectrum

$$E(\kappa) = \frac{4K}{\kappa_0}\left(\frac{\kappa}{\kappa_0}\right)^2 \exp\left(-2\frac{\kappa}{\kappa_0}\right), \tag{16}$$

where K is the turbulent kinetic energy (e.g., see Stanley et al., 2002). The wave number corresponding to the peak of the energy spectrum, κ_0, corresponds to the fundamental mode for the hyperbolic tangent shear layer, $\kappa_0 = 2\pi \times 0.033/\zeta$ (Monkewitz and Huerre, 1982). Since the fluctuations generated from the energy spectrum do not satisfy the continuity constraint, the velocity vector is projected onto a divergence-free space and then the resulting vector is added to the mean inlet velocity profile. Imposition of the disturbances as outlined above was important to rapidly amplifying the natural instabilities of the jets and developing a three-dimensional solution. In computations of the jets without any disturbances imposed on the inlet velocity profile the predicted fields were smooth, i.e., without fluctuations or three-dimensional structure. In addition, computations in which the initial velocity fluctuations were random, corresponding to a white-noise spectrum, the solutions did not sustain the initial perturbations, a feature consistent with the relatively low Reynolds number of the jets and proximity of the nozzle to the impinging surface.

The time history of the spatially-averaged (over the inlet plane) root-mean-square (rms) velocity fluctuations is illustrated in Fig. 3(a), the figure showing the traces for the unforced jets. The figure shows the chaotic nature of the velocity components (without correlation among the components) and isotropy, $u_{\mathrm{rms}} = v_{\mathrm{rms}} = w_{\mathrm{rms}}$. Fig. 3(b) shows the time- and span-averaged mean and rms u-velocity profiles along and near the inlets of each nozzle. Statistics were obtained by averaging the solutions over several hundred time units B/U_0, sufficient to ensure symmetry in the velocity statistics about $y/B = 0$. The figure also shows the co-flow applied for $|y/B| > 3.6$ and the rms level of the velocity across the inflow plane of $0.03U_0$ (except near the slot inlet for the forced jets shown in the right-hand frame of the figure), corresponding to approximately the value anticipated in the companion experiments.

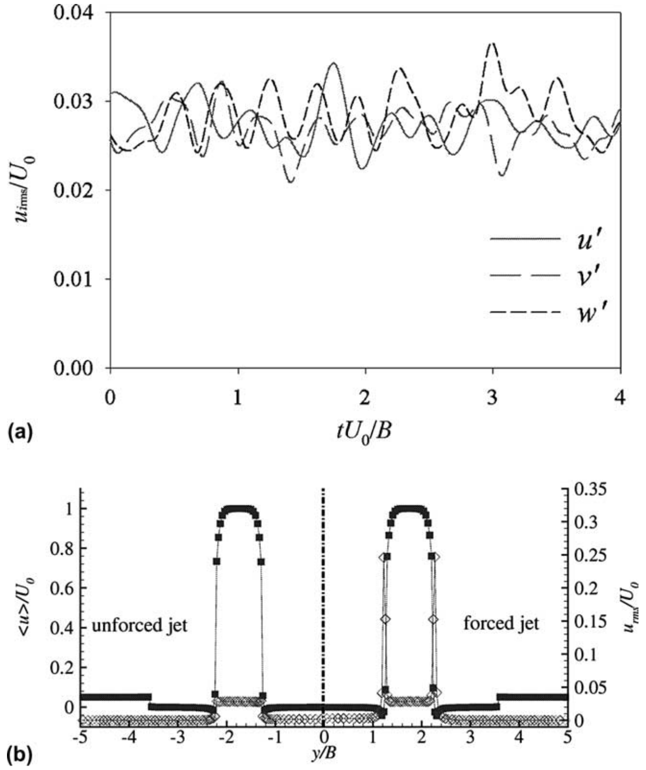

Fig. 3. Properties of inlet velocity in the LES: (a) rms velocity histories averaged over the inlet plane and (b) averaged inlet conditions. (left frame) Unforced jets and (right frame) forced jets. (■) Mean velocity and (◇) rms.

2.5. Experimental configuration

In this study, the LES predictions are compared to experimental measurements of the velocity field obtained using Laser Doppler Velocimetry (LDV) and Particle Image Velocimetry (PIV). The experimental setup is illustrated in Fig. 4 for the PIV measurements. A water jet issuing from two identical rectangular nozzles (width: $B = 10$ mm, aspect ratio 10:1) located in parallel (nozzle spacing: $s = 36$ mm). Forcing of the jets was achieved using injection and suction through slits along the nozzle exits, which were connected to syringes by silicone tubes. The syringes were actuated using stepping motors controlled by a PC.

The jets impinge onto a heated surface that is extended to $|y/B| = 5$ and is made of 20 μm thick stainless steel foil heaters with a 5 mm thick expanded polystyrene backing plate. The heater produces a constant heat flux generated by direct current. Eleven copper-constantan thermocouples, of which conjunctions are approximately 100 μm in diameter are embedded on the backside of the heater at intervals of 10 mm along the y direction. In evaluation of the heat transfer coefficient obtained via the measurements, losses due to effects of contact resistance, radiation, and foil heat conduction though the polystyrene were not taken into account. Estimates of these losses would lower the heat flux used to evaluate the Nusselt number by less than 3%.

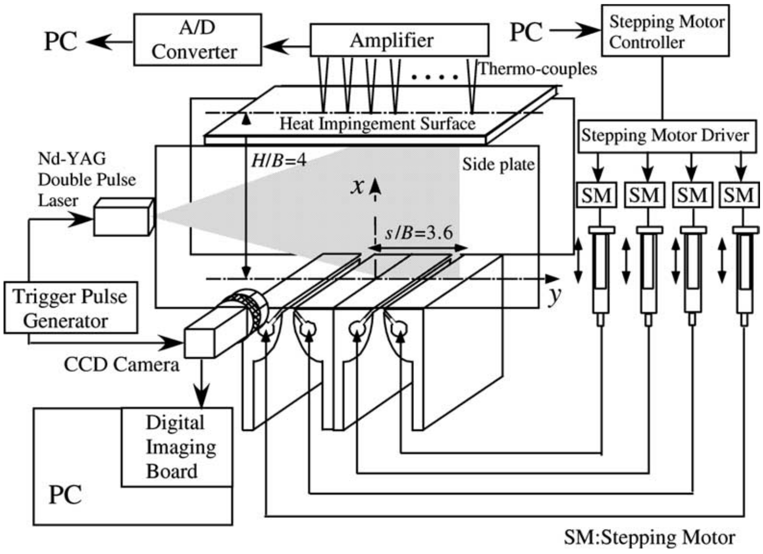

Fig. 4. Schematic of the experimental apparatus.

LDV is used to obtain detailed velocity distributions compared to the PIV which is used to provide planar measurements and to assist in interpretation of the flow field. Tracer particles having an average diameter of 12 μm were seeded into the working fluid in order to acquire the aforementioned measurements. The measuring volume of the LDV is $80 \times 80 \times 500\,\mu\mathrm{m}^3$. Data processing of the Doppler signal is performed using an FFT-based analyzer with a digital signal processor. The Doppler burst signal is digitized by an analog-to-digital converter and analyzed using a 128-point Fast Fourier Transform to obtain the frequency spectrum. The corresponding velocity is calculated from the peak frequency in the spectrum by an extended Gaussian fitting. The bias error was less than 0.2% for the fundamental frequency. Statistics were obtained by accumulation of 2000 samples over temporal periods much longer than any timescale in the flow. Repeatability was ensured by comparing the statistics from multiple trials (each of 2000 samples) and to assure convergence in the mean and second-order statistics shown below.

PIV measurements are acquired using a CCD camera which has a resolution of 1008×1018 pixels and double pulse Nd-YAG laser (30 mJ per pulse). The length of a pixel unit in the images corresponds to 71.4 μm in the actual measured field. The velocity vectors are calculated via cross-correlation of pairs of the double pulsed images using a hierarchical vector investigation algorithm. The interval of the double-pulse laser was adjusted to 6ms using a pulse generator. The sampling rate is 15 Hz. Sub-pixel interpolation is performed using Gaussian fitting of correlation maps. The statistical data is calculated from 1000 velocity vector maps. Uncertainty of the PIV velocity measurement was estimated ±1% for a 95% confidence interval.

3. Results

Predictions are obtained of both unforced and forced jets in order to assess the effect of injection/suction at the nozzle exit on flow structure and statistics. In the forced flows, the injection and suction profile is sinusoidal, prescribed as $\mid U_{\mathrm{f}} \mid = 0.5U_0 \sin(2\pi St \times t)$ where the Strouhal number St of 0.22 is used in the experiments and simulations (corresponding to a sinusoid of 1 Hz). The forcing applied to each jet are synchronized and without phase lag at any of the four injection/suction locations (i.e., at each side of the two jets).

The influence of mesh refinement was investigated via comparison of solutions obtained on two grids, the baseline mesh comprised of $64 \times 192 \times 32$ points and a finer mesh with refinement in the y direction for an overall grid size of $64 \times 256 \times 32$ points (in x, y, z). Fig. 5 shows the influence of the refinement on the mean and rms v-velocity, the profiles in the figure taken normal to the impinging wall. As shown in the figure, there are only small changes in the mean and fluctuating velocity profiles with refinement in the y direction. Fig. 5 also shows two distinct peaks in the rms velocity profile, correlated to the regions of large gradients in the mean velocity of the flow as it develops as a wall jet along the impinging surface.

Simulations of three-dimensional flow in two-dimensional geometries introduce some ambiguity through specification of the spanwise period (over which periodic boundary conditions are applied). The spanwise domain size of $3B$ for the current runs is in the range of other investigations of impinging jets using LES or DNS. In Abe and Suga (1998) the spanwise period in a single-jet impingement predicted using LES was $3B$. Tsubokura et al. (2002) used DNS to compute single-jet

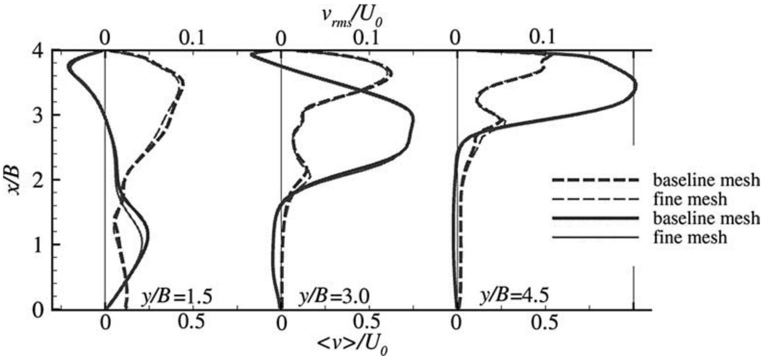

Fig. 5. Effect of grid refinement on the mean (solid line) and rms (dashed line) v-velocity profiles in the LES.

impingement using a spanwise dimension of πB. The influence of the spanwise period is investigated using simulations performed on a domain in which the spanwise dimension was increased to $5B$. For this test, the solution was discretized using 54 grid points along this dimension in order to maintain the same grid spacing in the spanwise direction as in the baseline runs. LES predictions of the v-velocity for this case compared to the baseline configuration are shown in Fig. 6. The figure shows that the mean values coincide and with a slight difference in the rms levels for the two cases, increasing confidence that the current domain of $3B$ is adequate for the present simulations.

Fig. 7 shows the instantaneous velocity and spanwise vorticity maps for both the unforced (in a) and forced (in b) jets from PIV measurements and the LES predictions. The figure shows that the computation resolves somewhat similar flow characteristics and vortical structures for each flow type. Comparison of the unforced and forced flows from the PIV and LES illustrates the strong influence of the forcing on the shear layer development downstream of the nozzle. It is also apparent from the figure that for both flow types the influence of the wall and mutual interactions of the jets are relatively strong, with the flows turning from the symmetry plane immediately downstream of the nozzle exit. In the unforced jets the PIV measurements indicate somewhat more significant interactions, as evidenced by a larger curvature of the jets compared to the LES prediction.

For the forced case in Fig. 7(b), both PIV and LES show that the forcing leads to a relatively rapid development of large-scale vortices in the shear layers, though the vortical rollup in the PIV measurement appears stronger than in the LES. The amplitude and waveform of the pulsing used to force the jets was not precisely measured in the experiments and Fig. 7(b) indicates a stronger effect of the forcing, e.g., as visualized through the development of more significant vortical structures downstream of the nozzles. In addition, compared to the unforced flow, Fig. 7(b) shows that the vector maps for the forced case are characterized by relatively more chaotic motions and larger velocities along the wall towards the symmetry plane $y/B = 0$ in the vicinity of the stagnation region (near $|y/B| = 3.1$), an effect that influences the local Nusselt number distribution as shown below (c.f., Fig. 14).

Instantaneous velocity vectors and temperature contours in the unforced and forced jets are depicted in Fig. 8. Comparison of the frames shows the strong effect of the forcing in enhancing mixing in the the region between the jets (roughly the region from $(x/B, |y/B|) = (0, 1.3)$ to the impinging surface). Advection of the heated fluid by the structures to the region outside

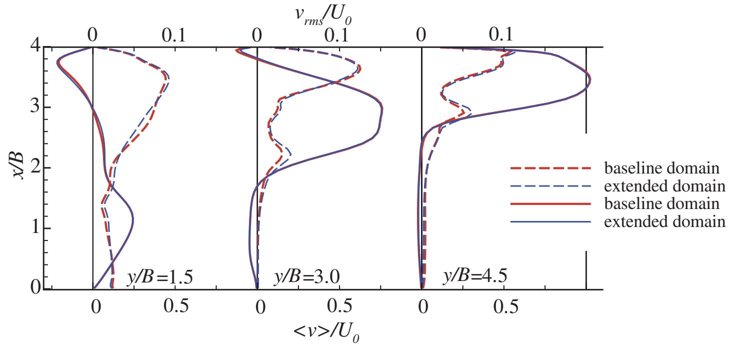

Fig. 6. Effect of the spanwise domain size on the mean (solid line) and rms (dashed line) v-velocity profiles in the LES.

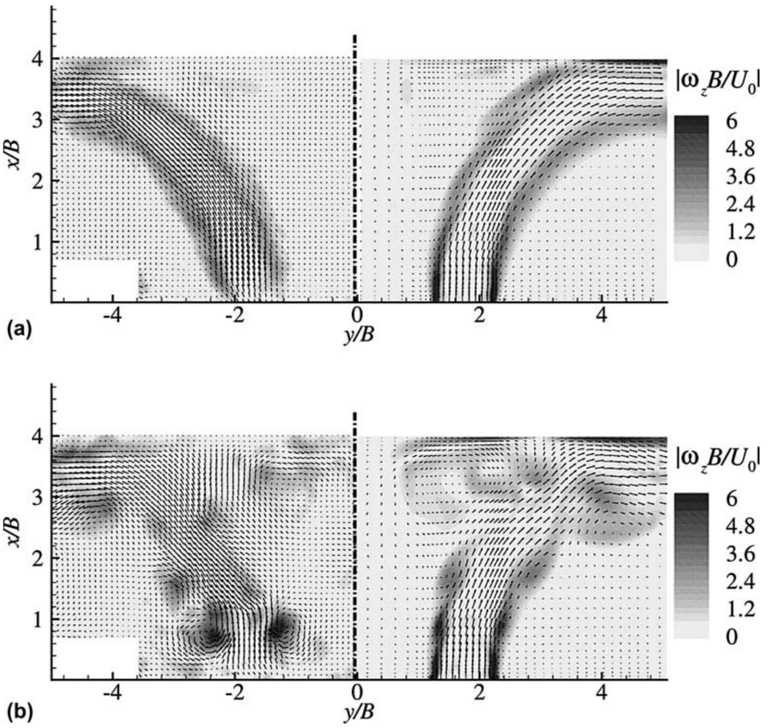

Fig. 7. Instantaneous velocity vector and contour map of the spanwise vorticity $|\omega_z|$. Left frame ($-y$ region): PIV measurement and right frame ($+y$ region): LES prediction: (a) unforced jets and (b) forced jets.

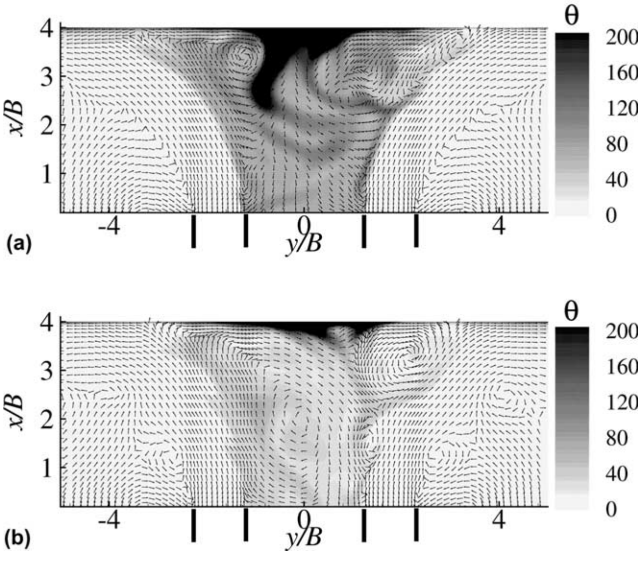

Fig. 8. LES prediction of the instantaneous velocity vectors and temperature contours: (a) unforced jets and (b) forced jets.

of the jets is more efficient in the forced case and lowers the temperature in the region between the jets.

Vorticity isosurfaces in the three-dimensional solutions for both flow types are illustrated in Fig. 9. The figure shows the relatively strong differences in the spanwise vorticity developing downstream of the nozzle exits, i.e., a sheet in the unforced flow (Fig. 9(a)) and relatively coherent spanwise structures in the forced case (Fig. 9(b)). The figure also shows the in-phase character of the spanwise structures in the forced flow, consistent with no phase lag in the forcing applied along the nozzle inlet. For both flow types, only the vortical structures in the inner region (nearer to the symmetry plane $y/B = 0$) impinge on the lower wall. The outer shear layers (i.e., at the outer periphery of each jet) do not impinge but instead are deflected away from the nozzle and develop further over the flow as it develops wall jets in the $+y$ and $-y$ directions.

Fig. 9 also shows the development of y-component ("streamwise") vorticity in the flow, prior to the impingement, for both the unforced and forced jets. The formation of these structures arises from the rib structure connecting consecutive spanwise vortical rollers, as depicted schematically in Fig. 10. In the forced case, straining of the spanwise structures is relatively strong compared to the unforced flow. Amplification of the disturbances entering through the inflow plane develop into coherent spanwise structures. In the dual impinging jets considered here, since the cores of each jet are deflected outwards, the rib structures in the shear layers which are nearer the symmetry plane $y = 0$ are strained and develop both in the unforced and forced cases, though are weaker in the unforced flow. As the jets impinge onto the lower wall, these vortices develop into streamwise structures, referred to as 'wall–rib structures' in Sakakibara et al. (2001). The vorticity in the structures becomes more intense as the flow impinges

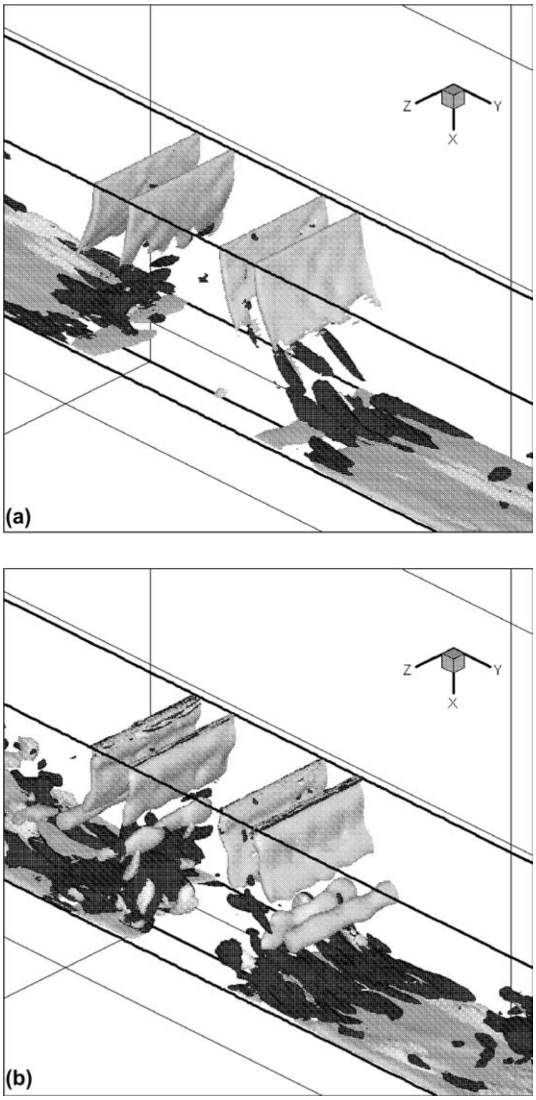

Fig. 9. Vorticity isosurfaces—LES prediction, (black) $|\omega_y| = 1.0$ and (dark gray) $|\omega_z| = 3.0$: (a) unforced jets and (b) forced jets.

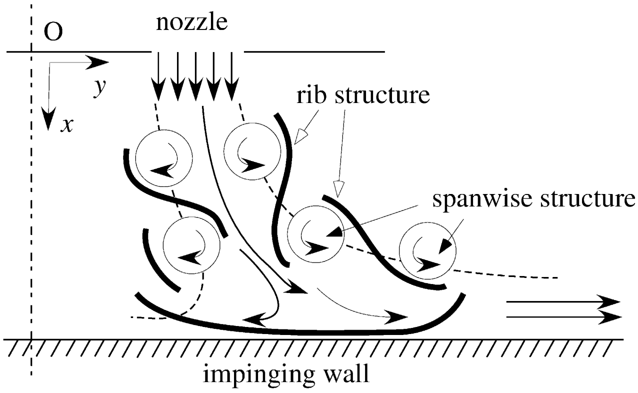

Fig. 10. Schematic of vertical structures in the impinging region for dual jets.

onto the wall, with regions of 'forward flow' (away from the nozzles) and 'reversed flow' (towards the symmetry plane), straining the structure from side to side (c.f., Fig. 10). Both the mean motion and spanwise vortical structures strain the wall–rib structures in the forced case (c.f., Fig. 10), leading to a more intense wall–rib structure in the forced flow compared to the unforced case.

Contours of the instantaneous streamwise (ω_y) vorticity in three x–z sections are shown in Fig. 11. In the plane $y/B = 3.3$, corresponding to the stagnation line and shown in Fig. 11(b) the relatively coherent streamwise vorticity is apparent, the counter-rotating structures possessing a lengthscale slightly smaller than the nozzle width B. Nearer and further from the plane $y/B = 3.3$ (Fig. 11(a) and (c)) the vortical structures remain relatively well defined, aspects that in turn influence the surface transfer characteristics, as noted by Sakakibara et al. (1997), though the most pronounced effects occur closest to the stagnation line.

Contours of the u- and v-velocity components from the LES are shown in Fig. 12. Averaged quantities are computed by sampling over time and in addition over the statistically homogeneous z direction and folded about $y = 0$. Both velocity components show that near the nozzles there are not substantial differences in the mean flow between the forced and unforced jets. With

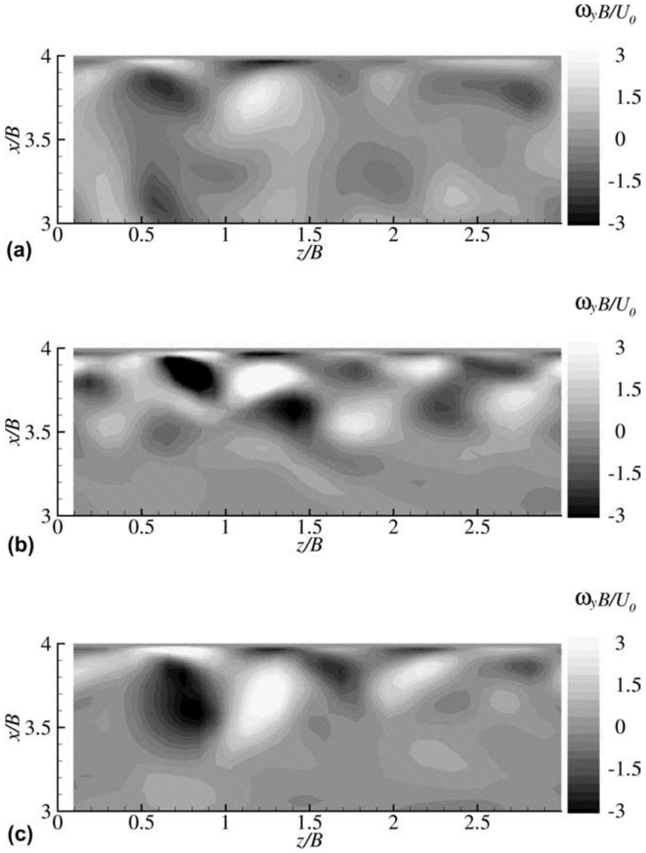

Fig. 11. $x - z$ sections of instantaneous ω_y distributions in the forced jets—LES prediction: (a) $y/B = 2.3$; (b) $y/B = 3.3$ (on the stagnation line) and (c) $y/B = 4.3$.

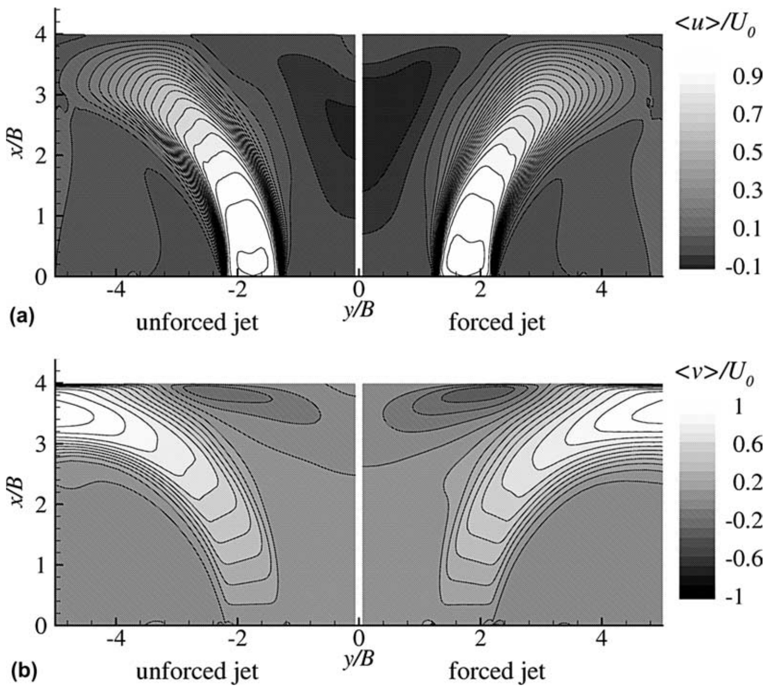

Fig. 12. Mean velocity contours (note that for the unforced jet in the left frame the v velocity is shown with opposite sign in order to use an identical contour range as for the forced jet)—LES prediction: (a) $\langle \bar{u} \rangle / U_0$ and (b) $\langle \bar{v} \rangle / U_0$.

evolution towards the impinging wall the mean velocities indicate a greater spreading in the forced jets, especially in the region where the flow is developing as a wall jet. In addition, substantial differences are visible near the wall and close to the symmetry plane $y/B = 0$. In the forced case there is a larger mean flow back towards the nozzles and a stronger reversed flow in the v component close to the surface.

Fig. 13(a) shows the comparison of the mean u-velocity profiles obtained from the experimental measurements using LDV and the LES predictions. Near the nozzle, the LES prediction of the mean velocity for the unforced flow (left frame of Fig. 13(a)) show some agreement with the measurements, though even at the location nearest the nozzle, $x/B = 0.5$, it is apparent the shear layers are developing differently in the measured flow compared to the simulation. With further evolution of the jets to $x/B = 2.0$, Fig. 13(a) shows that the agreement between simulation and experiment is adequate in the shear layers, though the LES prediction yields peak values that are lower than measured. At $x/B = 3.0$, the peak in the velocity profiles from the LES and experiments are shifted with the LES profile outboard of the measurement. In general, these features are consistent with the visualizations shown in Fig. 7, which also indicated a different development in the measured jet compared to the simulated one.

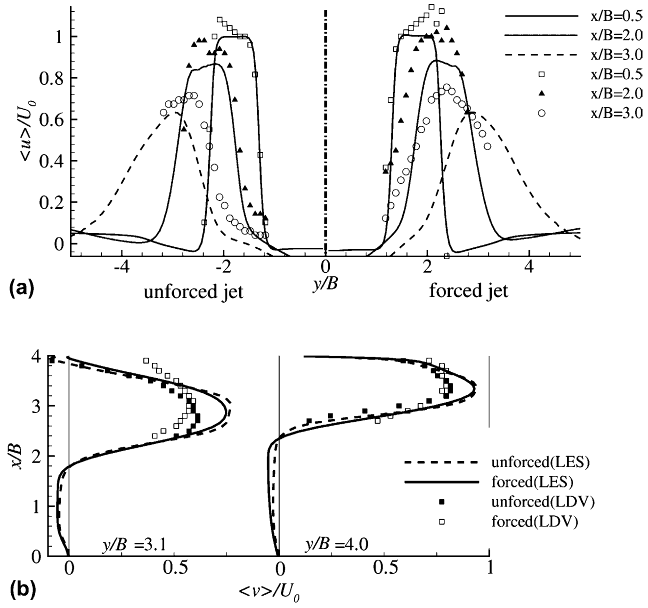

Fig. 13. Mean velocity. Lines are the LES predictions, symbols are the LDV measurements: (a) x-component near the nozzle region, left side: unforced jet and right side: forced jet; (b) wall jet region.

Fig. 13(a) also shows discrepancies between the LES and measurements in the forced flow (right frame of the figure). As also observed in the unforced jet, the shear layers are developing differently in the experiment compared to the LES, an effect that probably arises from differences in the inflow conditions between the simulation and experiment. At $x/B = 2.0$ and $x/B = 3.0$, the figure shows the mean u profiles predicted by the LES in the forced case are rather different compared to the measurements. While the spreading of the jets appears somewhat similar, the profiles in the LES again possess lower peaks and are displaced further from the symmetry plane than indicated by the measurements. The mean v-velocity profile in the wall jet region is shown in Fig. 13(b). In the unforced jets, the LES prediction exhibits reasonable agreement with the distribution in the shear layers, both near the wall in the outer region, though shows higher peak velocities than indicated by the measurements. In the forced flow, the LES predictions yield mean v profiles that show only small differences compared to the unforced case. The experimental measurements in Fig. 13(b) show stronger effects of the forcing, especially at $y/B = 3.1$ and in the outer shear layers at both $y/B = 3.1$ and $y/B = 4.0$.

The Nusselt number distribution along the impinging wall is shown in Fig. 14. The error bars indicate the 95% confidence interval in the measurements. There is good agreement between the LES and measurements in the vicinity of the stagnation line, $y/B = 3.3$, for both the unforced and forced cases. Figure 14 shows that the LES prediction of the peak Nusselt number increases by about 10% at the stagnation line under the influence of forcing and that from the symmetry plane to the stagnation line both the LES and measured Nusselt numbers indicate an enhancement in the mean heat transfer by the forcing. The increase in the heat transfer is consistent with the earlier observations of the temperature field between the jets that showed the influence of the forcing resulted in substantially greater mixing and lower temperatures due to the heated fluid being ejected from the inner region between the jets to regions outside the jets. In addition, the relatively stronger streamwise vortices as observed in the flow visualizations (c.f., Figs. 10 and 11) also enhance heat transfer, Fig. 14 showing that there is a measurable change in the mean. For increasing y/B past the stagnation line the LES predictions show less difference in the Nusselt number for the forced and unforced jets. The measurements at $y/B = 5$ indicate possibly greater variations between the two flow types, though the differences are within the error bars.

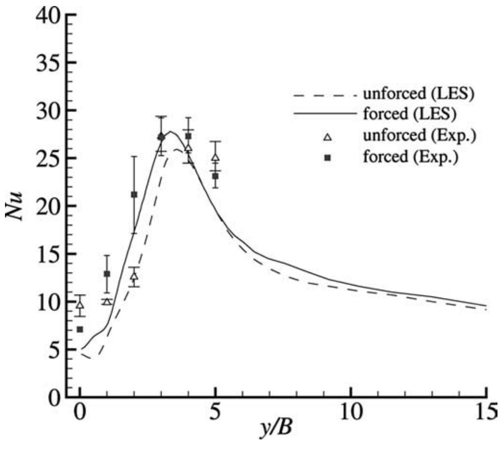

Fig. 14. Nusselt number on the impinging wall.

Compared to the earlier study of Hishida and Sakakibara (2000) that focused on single-jet impingement, both the present work as well as that of Hishida and Sakakibara (2000) show that streamwise vorticity, leading to the formation of wall–rib structures are important to the overall flow and heat transfer signature on the impinging wall. In the dual-jet impingement considered here the region between the stagnation lines, i.e., between $-3 < y/B < 3$, is characterized by lower heat transfer rates than observed in the single-jet case, this feature connected to the mutual interactions of the jets that obviously cannot occur in the single-jet case.

4. Conclusions

In the present study, two planar impinging jets were investigated using simulations and experimental measurements. Both unforced and forced cases were considered, the forcing providing a mechanism for generating coherent structures in the jet shear layers which subsequently interact with the wall. The increase of the heat transfer in the region between the jets resulted from greater mixing and ejection of heated fluid from the inner region between the jets to regions outside the jets. For both the unforced and forced flows the LES predictions show the jet develops streamwise vorticity, the turbulent inflow condition providing disturbances that the jets efficiently amplify.

In general, the LES predictions of the velocity and Nusselt number distribution along the impinging wall show some regions of agreement in the unforced flow. In the forced case, however, there are differences between the two techniques used to investigate the flow. The Reynolds number for the current configuration is moderate, an aspect that should increase the fidelity of the LES since modeling errors are less significant compared to higher-Reynolds number applications, though application of other sub-grid closures probably represents a useful exercise to gauge the sensitivity of LES predictions to the physical modeling. That differences are apparent between the simulation and experiment reflects the difficult aspects of the flow connected more to the configuration and boundary conditions, as opposed to turbulence modeling and numerical errors arising from the discretization and factors such as the spanwise period.

The simulations considered a section of the experimental facility, applying periodic boundary conditions along the spanwise direction. While the simulations performed using a larger spanwise dimension showed good agreement with the shorter spanwise period, end effects that are present in the experiment were not incorporated into the computational model, a practical constraint imposed by available resources. Slight differences in the details to forcing the flow between the simulation and experiment also contribute to the differences observed in the statistical features of the flow downstream of the nozzles. Future studies should consider more detailed investigations of the forcing in order that the inlet conditions between simulation and experiment match as closely as possible.

Other aspects such as including a portion of the nozzle through which fluid is introduced to the domain might also improve the reproduction of the experimental facility by the simulations. Possible influences of receptivity cannot be accurately reproduced for the given simulation domain. While likely not a significant error source in the forced flow, incorporating such aspects into the computational model will increase the fidelity of the predictions and provide a more useful tool for future flow-control investigations. All of these features are important considerations because of the sensitivity of jets to the inlet conditions—numerical tools used to assist in understanding and developing flow control strategies must necessarily replicate such effects.

In spite of these considerations, the capacity of techniques such as LES to resolve a range of spatial and temporal scales is apparent in the simulations performed in this effort and should enable the technique to eventually be an effective complement to measurements for flow control applications. An aspect of the system not thoroughly addressed in the present effort though useful for future control applications is a deeper investigation of the 'streamwise' vortical structures and their signature on the impinging wall. The dynamics of these structures, which are sensitive to the forcing and therefore excellent candidates for control, should be more thoroughly studied using techniques such as phase averaging to understand not only the statistical properties but also the structural features.

Acknowledgements

The second author (KY) gratefully acknowledges the Grant in Aid for the 21st Century Center of Excellence for "System Design: Paradigm Shift from Intelligence to Life" from the Ministry of Education, Culture, Sport, and Technology in Japan, by which the present work was partially supported. The third author (KDS) is pleased to acknowledge the Center for Smart Control of Turbulence funded by the Ministry of Education, Culture, Sport, and Technology in Japan, for financial support as a visiting professor in 2003. The Navier–Stokes solver used in this study was developed by Professor Takeo Kajishima of Osaka University, whose work is gratefully acknowledged.

References

Abe, K., Suga, K., 1998. Large-Eddy simulation of passive scalar in complex turbulence with flow impingement and flow separation. Trans. JSME Ser. B 65 (632), 1395–1402 (in Japanese).

Baughn, J., Shimizu, S., 1989. Heat transfer measurements from a surface with uniform heat flux and an impinging jet. J. Heat Transfer 111, 1096–1098.

Behnia, M., Parneix, S., Shabany, Y., Durbin, P.A., 1999. Numerical study of turbulent heat transfer in confined and unconfined impinging jets. Int. J. Heat Fluid Flow 20, 1–9.

Chester, S., Charlette, F., Meneveau, C., 2001. Dynamic model for LES without test filtering: quantifying the accuracy of Taylor series approximations. Theoret. Comput. Fluid Dyn. 15, 165–181.

Crow, S.C., Champagne, F.H., 1971. Orderly structure in jet turbulence. J. Fluid Mech. 48, 547–591.

Germano, M., Piomelli, U., Moin, P., Cabot, W.H., 1991. A dynamic subgrid-scale eddy viscosity model. Phys. Fluids 3 (7), 1760–1765.

Hishida, K., Sakakibara, J., 2000. Combined planar laser-induced fluorescence-particle image velocimetry technique for velocity and temperature fields. Exp. Fluids 29 (Suppl.), S129–S140.

Hwang, S.D., Cho, H.H., 2003. Effects of acoustic excitation positions on 17 heat transfer and flow in axisymmetric impinging jet: main jet excitation and shear layer excitation. Int. J. Heat Fluid Flow 24, 199–209.

Kajishima, T., 1999. Finite-difference method for convective terms using non-uniform grid. Trans. JSME Ser. B 65 (633), 1607–1612 (in Japanese).

Leonard, B.P., 1979. A stable and accurate convective modelling procedure based on quadratic upstream interpolation. Comput. Methods Appl. Mech. Eng. 9, 59–98.

Lilly, D.K., 1992. A proposed modification of the Germano subgrid-scale method. Phys. Fluids 4 (4), 633–635.

Liu, T., Sullivan, J.P., 1996. Heat transfer and flow structures in an excited circular impinging jet. Int. J. Heat Mass Transfer 39 (17), 3695–3706.

Lytle, D., Webb, B., 1994. Air jet impingement heat transfer at low nozzle-plate spacings. Int. J. Heat Mass Transfer 37, 1687–1697.

Monkewitz, P.A., Huerre, P., 1982. Influence of the velocity ratio on the spatial instability of mixing layers. Phys. Fluids 25, 1137–1143.

Sakakibara, J., Hishida, K., Maeda, M., 1997. Vortex structure and heat transfer in the stagnation region of an impinging plane jet (simultaneous measurements of velocity and temperature fields by digital particle image velocimetry and laser-induced fluorescence). Int. J. Heat Mass Transfer 40 (13), 3163–3176.

Sakakibara, J., Hishida, K., Phillips, W.R.C., 2001. On the vortical structure in a plane impinging jet. J. Fluid Mech. 434, 273–300.

Stanley, S.A., Sarkar, S., Mellado, J.P., 2002. A study of the flow-field evolution and mixing in a planar turbulent jet using direct numerical simulation. J. Fluid Mech. 450, 377–407.

Tsubokura, M., Kobayashi, N., Taniguchi, N., 2002. Numerical study on the difference of the eddy structures between plane and round impinging jets. In: Proceedings of the 5th International Symposium on Engineering Turbulence Modelling and Measurements, Mallorca, Spain, 16–18 September 2002.

Yamamoto, K., Nozaki, A., Hishida, K., 2002. Heat transfer control from a plate by parallel synthetic impinging jets. Proceedings of the 12th International Heat Transfer Conference, Grenoble, France, August 18–23. Elsevier, Amsterdam (Also available in CD-ROM).

Zaman, K.B.M.Q., Hussain, A.K.M.F., 1981. Turbulence suppression in free shear flows by controlled excitation. J. Fluid Mech. 103, 133–159.